The Astrophysical Journal, 983:102 (12pp), 2025 April 20 https://doi.org/10.3847/1538-4357/adbf8b

Revealing the CME Impact on the Martian Nightside Ionosphere Based on MAVEN and Tianwen-1 Observations

Longhui Liu[1,2], Xinzhi Qiu[1,2], Yiqun Yu[1,2], Wudi Luo[3], Xin Wang[1,2], Jinbin Cao[1,2], Cunhui Li[4], YuMing Wang[5,6], and TieLong Zhang[6,7]
[1] School of Space and Earth Sciences, Beihang University, Beijing, People's Republic of China; yiqunyu17@gmail.com
[2] Key Laboratory of Space Environment Monitoring and Information Processing, Ministry of Industry and Information Technology, Beijing, People's Republic of China
[3] School of Astronautics, Beihang University, Beijing, People's Republic of China
[4] Science and Technology on Vacuum Technology and Physics Laboratory, Lanzhou Institute of Physics, Lanzhou, People's Republic of China
[5] National Key Laboratory of Deep Space Exploration/School of Earth and Space Sciences, University of Science and Technology of China, Hefei, People's Republic of China
[6] CAS Center for Excellence in Comparative Planetology/CAS Key Laboratory of Geospace Environment/Mengcheng National Geophysical Observatory, University of Science and Technology of China, Hefei, People's Republic of China
[7] Space Research Institute, Austrian Academy of Sciences, Graz, Austria
Received 2024 November 12; revised 2025 March 6; accepted 2025 March 10; published 2025 April 11

Abstract

Due to the absence of an Earth-like dipole magnetic field, the impact of coronal mass ejections (CMEs) on the Martian nightside ionosphere differs from that on Earth and is still not well understood. This study investigates the responses in the Martian nightside ionosphere to a CME event that occurred on 2022 August 30 using observations from Tianwen-1 and Mars Atmosphere and Volatile EvolutioN. The ion density in the upper Martian nightside ionosphere between 200 and 500 km decreases when two successive CMEs hit the induced Martian magnetosphere, with a brief density recovery between the two CMEs. This suggests that ion density in the Martian nightside ionosphere between 200 and 500 km decreases as the intensity of CMEs increases. The primary cause of the observed decrease in the nightside ion density is likely due to the enhanced magnetic field pressure above the Martian ionosphere during CMEs, which facilitates ion escape from the dayside ionosphere; this subsequently reduces the amount of ions transported to the nightside ionosphere, thereby leading to a decrease in ion density on nightside. Furthermore, hemispheric asymmetry is found in the ionospheric response, indicating that the crustal magnetic fields in the southern hemisphere may play a role in slowing down the reduction of ion density. This study expands the comprehensive description of the impact of a CME event on different regions of Mars and its underlying mechanisms.

Unified Astronomy Thesaurus concepts: Solar coronal mass ejections (310); Planetary ionospheres (2185); Mars (1007)

1. Introduction

Coronal mass ejections (CMEs) are spectacular eruptions in the solar atmosphere and expand to interplanetary space (P. F. Chen 2011). The CME exhibits a complex magnetic structure characterized by low plasma β and low ion temperature, and drives a high-speed, high-density shock front. CME arrival is typically identified through observations of strong magnetic fields, bidirectional streaming of electrons, high velocities in the affected regions, and subsequent velocity decreases (N. Gopalswamy et al. 2000; C. T. Russell & A. A. Shinde 2005; R. F. Wimmer-Schweingruber et al. 2006; C. Shen et al. 2014; Y. Wang et al. 2014; F. Shen et al. 2022; L. Ram et al. 2023). As one of the most common large-scale disturbances in the heliosphere, CMEs drive many space weather phenomena in planetary environments. On Earth, CMEs may lead to geomagnetic storms, ionosphere anomalies, reconnections along the magnetopause, and other space weather effects (T. E. Moore et al. 1999; C. Wang et al. 2016; P. Hess & J. Zhang 2017). Unlike Earth, Mars does not have a global dipole magnetic field, so the solar wind can approach much closer where it interacts directly with the Martian atmosphere, potentially leading to a more efficient loss of planetary ions from the atmosphere (D. A. Brain et al. 2015). H. J. Opgenoorth et al. (2013) demonstrated that the dynamic pressure of the solar wind appears to be the primary controlling factor for ion acceleration through the comparison of ion acceleration characteristics before and after the CME passage by Mars. The prolonged duration of CMEs extends the persistence of dynamic pressure pulses. Upon reaching Mars, CMEs can lead to significant compression of the Martian magnetosphere and ionosphere, as well as the acceleration of ionospheric ions, increasing ionospheric ion outflow and loss (Y. Chi et al. 2023; L. Ram et al. 2023).

The ionosphere is the plasma component of the upper atmospheres of planets, satellites, and small bodies within the solar system. Martian neutral atmosphere is predominantly composed of CO_2, and its ionosphere is primarily characterized by molecular ions, O_2^+ being the dominant one. The two main sources of O_2^+ (S. A. Haider 1997) in the Martian ionosphere are:

$$CO_2^+ + O \longrightarrow O_2^+ + CO \quad (1)$$

$$CO_2 + O + \longrightarrow O_2^+ + CO. \quad (2)$$

According to previous studies (E. Dubinin et al. 2012; Z. Girazian et al. 2017), there is a day–night asymmetry in the Martian ionosphere. In the 1970s, Viking Landers first observed the ionosphere on the dayside of Mars, indicating that

the photoionization of CO_2 by solar photons is the main source of plasma on the dayside (W. B. Hanson et al. 1977; R. H. Chen et al. 1978; P. Withers 2009). After subsequent extensive studies, it is currently believed that the two main sources of plasma in the nightside ionosphere are collisions of precipitating electrons and day-to-night transport (e.g., S. A. Haider 1997; J. Cui et al. 2015).

Due to the direct interaction of the solar wind with the Martian atmosphere and ionosphere, as well as the compression of the magnetosphere, the dayside ionosphere is directly affected by CME events. This impact can alter one of the aforementioned primary sources of the nightside ionosphere, thereby affecting the ion density in the nightside ionosphere. Numerous studies have demonstrated that, during CME events, the particle density in the nightside ionosphere below 200 km exhibits an increase, particularly in electron density, which is likely a consequence of enhanced collisional ionization caused by the enhanced precipitation of energetic particles (D. Ulusen et al. 2012; F. Duru et al. 2017; Y. Harada et al. 2018). However, when focusing on the upper ionosphere between 200 and 500 km, particle density significantly decreases due to ionospheric compression and enhanced ion escape (S. V. Thampi et al. 2018; L. Ram et al. 2023; B. Yu et al. 2023). In some studies, an observed increase in particle density in the upper ionosphere (the altitude range between 400 and 800 km) has been noted (F. Duru et al. 2017). F. Duru et al. inferred that this may result from the plasma escape process from Mars, during which escaping particles with high electron density and velocity are detected by spacecraft. The increase does not represent the state of the ionosphere after a CME passage but is a temporal pathway during its escape. Following the escape, the ionosphere density is depleted, consistent with previous studies.

Additionally, as Mars exhibits significant and unevenly distributed crustal remanent magnetization, the strong crustal magnetic fields can influence the interaction between the proximate solar wind and the Martian atmosphere, playing a crucial role in balancing solar wind pressure (e.g., J. E. P. Connerney et al. 2015) and in influencing energy transfer between the solar wind and Martian system via mini-magnetopause reconnection (e.g., J. Burch et al. 2016; J. Halekas et al. 2017a; R. Lin et al. 2024; X. Qiu et al. 2024b). These crustal magnetic fields are also found to contribute to hemispherical asymmetry in the ionospheric density distribution and ion precipitation (E. Dubinin et al. 2016; X. Qiu et al. 2024a). However, due to constraints imposed by spacecraft orbits, it is challenging to simultaneously discern variations in the upstream conditions of an entire CME event and different ionospheric responses across the northern and southern hemispheres on Mars.

Between 2022 August 30 and September 2, Tianwen-1 and Mars Atmosphere and Volatile EvolutioN (MAVEN) observed a CME event upstream from Mars, which lasted for approximately 3 days. The Tianwen-1 and MAVEN orbits during the event are illustrated in Figure 1. It can be seen that except for orbiting in the solar wind and induced Martian magnetosphere, MAVEN also crossed the Martian nightside ionosphere, inbound from the south and outbound in north, with almost the same dwell time in both hemispheres. On the other hand, Tianwen-1 passed through the dayside upper ionosphere multiple times in addition to its orbit in the solar wind. These two spacecraft missions provide an opportunity to examine the hemispherical variations in the Martian nightside ionosphere in response to the CME, and to

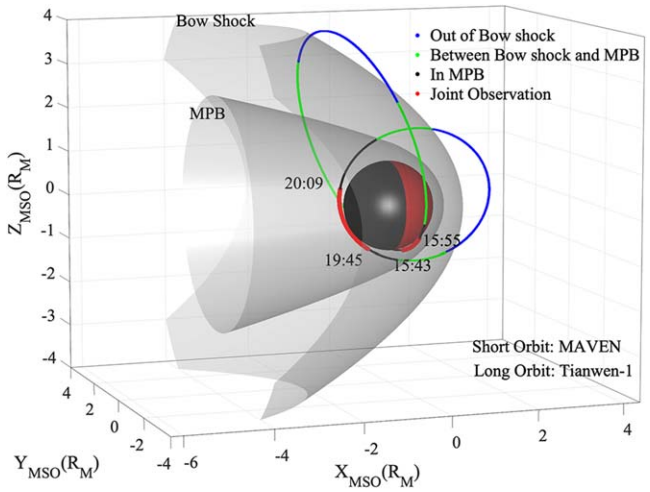

Figure 1. Orbits of Tianwen-1 and MAVEN on 2022 August 30. The flatter ellipse is Tianwen-1's orbit, while the other is MAVEN's orbit. The blue lines are the trajectories outside the bow shock; the green lines are the trajectories between bow shock and magnetic pile-up boundary (MPB); the black lines are the trajectories inside MPB; and the red lines are the trajectories that intersect with the ionosphere at altitudes below 500 km. The gray boundaries represent the bow shock and MPB, plotted based on the static empirical model by J. Trotignon et al. (2006).

elucidate the drivers in the solar wind and the mechanisms influencing both the dayside and nightside ionosphere. Specifically, this study investigates the response of the nightside upper ionosphere between 200 and 500 km during the CME event, and further compares the hemispherical differences between the northern and southern hemispheres. Section 2 provides a brief overview of the satellite data and simulation models employed. Section 3 details the identification of CME events through simulations and combined observations. Section 4 discusses the response of Martian nightside ionosphere and the regional variations observed. Section 5 provides a detailed observational analysis and explanation of the mechanisms influencing the event.

2. Data and Model Description

To analyze the solar wind condition and ionospheric responses, multiple instruments on board the MAVEN spacecraft (B. M. Jakosky et al. 2015b), Tianwen-1 (Y. Zou et al. 2021) and the Parker Solar Probe (PSP; N. Fox et al. 2016) are utilized. The solar wind data, including velocity, dynamic pressure and low to medium energy proton flux (which covers a broad energy range of 5 eV–25 keV for solar ions), are obtained from the MAVEN/Solar Wind Ion Analyzer (SWIA) in the data set of onboard moment survey telemetry and onboard survey energy spectra (J. S. Halekas et al. 2013, 2017b). The magnetic field data are obtained from the MAVEN/Magnetometer (MAG) in the data set of Sun-state coordinates data collection (J. E. P. Connerney et al. 2015). The data of electron pitch-angle distributions are obtained from the MAVEN/Solar Wind Electron Analyzer (SWEA) in the data set of archive rate electron pitch-angle distributions data collection (D. Mitchell et al. 2016).

Since 2021 November 13, the Mars Orbiter Magnetometer (MOMAG) instrument on Tianwen-1 has been regularly measuring the magnetic field from the solar wind to the magnetic pile-up region around Mars (K. Liu et al. 2020; Y. Chi et al. 2023; Y. Wang et al. 2023; Z. Zou et al. 2023;

G. Wang et al. 2024). The magnetic field data are obtained at a frequency of 1 Hz derived from the full-resolution source data to calculate the magnetic pressure. The Mars Energetic Particle Analyzer (MEPA) instrument on board Tianwen-1 is designed to measure and analyze high-energy charged particles in the Martian space environment, as well as in the interplanetary space between Earth and Mars (S. Tang et al. 2020; C. Li et al. 2021; S. Fu et al. 2022). We utilize the high-energy proton flux data from MEPA, which covers an energy range of 2–100 MeV with a time resolution of 4 s. The proton data are calibrated according to the methods provided by the payload development team, during which the time resolution is reduced to 1 min.

To identify the CME event, we utilize the Wang–Sheeley–Arge (WSA)-ENLIL+Cone model from the ENLIL Solar Wind Prediction (from Community Coordinated Modeling Center, NASA) to track the planetary positions, plasma feature, compressed streams, and interplanetary magnetic field over the heliosphere (C. N. Arge & V. J. Pizzo 2000; D. Odstrcil 2003; M. Mays et al. 2015). The WSA model has three components. The utilized component is the field solution to generate a wind speed by an empirical formula. The input parameters of WSA model are photospheric magnetograms from a range of sources, including daily updated synoptic maps, with their modifications and gaps filled by previous Carrington rotations or interpolation (C. N. Arge & V. J. Pizzo 2000). ENLIL is a time-dependent 3D MHD model of the heliosphere. It can accept boundary condition information from the WSA model and solves equations for plasma mass, momentum and energy density, and magnetic field, using a flux-corrected-transport algorithm (G. Tóth & D. Odstrčil 1996; D. Odstrčil & V. Pizzo 1999; D. Odstrcil 2003). Furthermore, the outer radial boundary must be set to 21.5 solar radii to combine the WSA model with the ENLIL model and complete the simulation of a CME event by generating a coronal field solution. This study obtained the simulation results of the solar wind velocity over the time range of the event, stored in the data tree of the WSA-ENLIL+Cone model.

While using the WSA-ENLIL model, we find that the CME in this study passed through PSP, therefore we use the partial moments of the proton distribution function in the Solar Probe Analyzer (SPAN) Ion instrument (R. Livi et al. 2022) and the electron pitch-angle distributions of the SPAN Electron instrument (P. L. Whittlesey et al. 2020) on board PSP to identify the passage of the CME event.

The data of Martian ionosphere are obtained from the Neutral Gas and Ion Mass Spectrometer (NGIMS) on board MAVEN (P. R. Mahaffy et al. 2015), which is designed to measure the ions and neutrals of the Martian atmosphere. The level 2 data of NGIMS are used in analyzing the response of Martian nightside ionosphere. The data of NGIMS collected in the data set of MAVEN in situ Key Parameters with a resolution of 4 s in version_v19, revision number_r01 (v19_r01) are used in analyzing hemispheric differences in the Martian nightside ionosphere in Section 4.

3. Observation and Simulation of the CME Event

A CME event observed by Tianwen-1 from 2022 August 30 to 2022 September 2 is investigated. For convenience, we abbreviate this as the August 30 event.

Figures 2(b) and (c) show the energetic protons flux and the intensity of magnetic field observed by Tianwen-1 during the event. The blue portion in Figure 2(c) represents the interplanetary magnetic field in the solar wind. The substantial enhancement of energetic proton flux (marked in pink and green shadows, II and IV) suggests the arrival of a solar energetic particles (SEP) event (J. Semkova et al. 2023). The high-energy (~2–100 MeV) proton flux remained elevated for several days, indicating that this was a large gradual SEP event (D. V. Reames et al. 1997; J. Zhang et al. 2024). In large gradual SEP events, the high-energy particles observed are typically regarded as being accelerated by shock waves driven by CMEs, with the flux peaking at the nose of the shock (H. V. Cane et al. 1988; D. V. Reames et al. 1997; F. Duru et al. 2017). The enhancement of the interplanetary magnetic field (marked in blue in Figure 2(c)) during the SEPs indicates that a CME event probably occurs simultaneously. Figure 2(a) presents the position of Tianwen-1 away from the center of Mars, in radii, indicating that each brief decrease in the energetic proton flux corresponds to Tianwen-1 moving toward Mars. This decrease is attributed to Tianwen-1 entering the magnetosphere and ionosphere, resulting in decrease in the detectable high-energy proton flux.

The proton flux remained at a high level from August 30 to September 2 before declining, which indicates the arrival and departure of CMEs in the near-Mars environment. It is noted that there were two phases during which the flux remained at a high level (marked as II, IV in Figure 2(b)), with multiple flux peaks appearing in phase IV. Given that the flux remained elevated throughout phase IV, we classify it as a sustained phase with an extended duration. We preliminarily infer that during this event, the Sun experienced multiple consecutive CMEs, resulting in the formation of this long-lasting CME event. To study the specific impact of August 30 event, this study separates the event into five phases: Phase I denotes the pre-event period; Phase II and Phase IV correspond to the phases with enhanced flux in the two successive CME events; Phase III signifies the brief recovery phase of solar wind conditions occurring between these two CME events; Phase V represents the recovery phase subsequent to the conclusion of the CME events, during which the Martian space environment gradually returns to a quiet state.

To further ascertain that the event is comprised of two consecutive CMEs, we investigate additional measurements from MAVEN. Figures 3(a)–(e) present the MAVEN observations during phases I–V characterized by their respective features. The solar wind conditions observed by MAVEN include energy spectrograms of low-energy protons from 26 eV to 23 keV; ion velocity and density (assuming the ions are solely protons); magnetic field intensity; and pitch-angle distributions of 100–500 eV electrons. Upon the arrival of the CME at 11:30 UT on August 30, as shown in Figure 3(a), the proton flux increases across a wide energy range around 1 keV, suggesting heating. The solar wind velocity and density show significant enhancement from ~400 to ~600 $\mathrm{km\,s^{-1}}$ and from ~2 to ~10 $\mathrm{cm^{-3}}$, respectively, which indicates the occurrence of a CME event (B. M. Jakosky et al. 2015a). Meanwhile, the magnetic field fluctuates significantly and enhances compared with pre-CME time. Figures 3(b) and (d) respectively represent a single orbit in Phase II and Phase IV. The proton energy spectrum maintains at a high-level flux over a wide energy range, with both solar wind velocity and proton density remaining high at ~500 $\mathrm{km\,s^{-1}}$ and ~20 $\mathrm{cm^{-3}}$ respectively, while the magnetic field strength still exceeds that of the quiescent period and even becomes strengthened. Meanwhile, electron pitch-angle

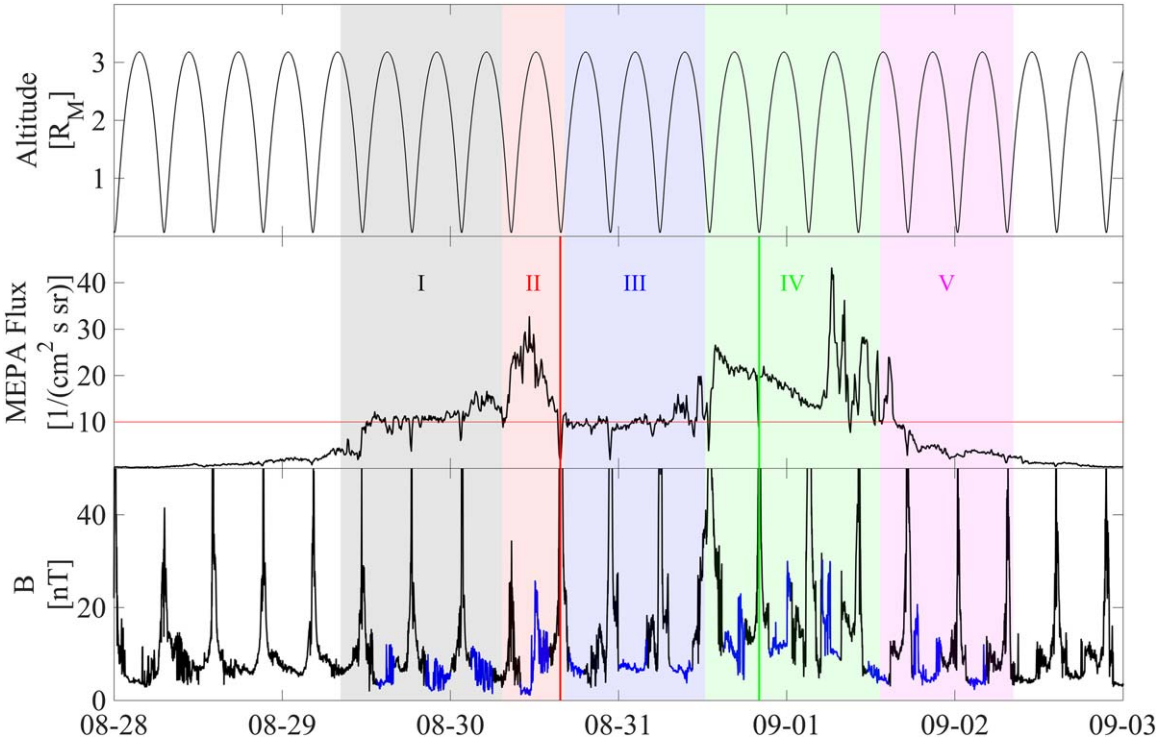

Figure 2. (a) The altitude of Tianwen-1 spacecraft, measured in radius. (b) Integrated flux of energetic protons of 2–100 MeV observed by Tianwen-1 payload MEPA. Five distinct phases (I–V) are chosen based on the intensity of the CME. (c) The intensity of magnetic field observed by the Tianwen-1 payload MOMAG. The blue portion represents the region in the solar wind.

distributions in the bottom image of Figures 3(b) and (d) illustrates the bidirectional streaming of electrons, one of the key features of CME events (C. Shen et al. 2014). The flux around 0° and 180° pitch angles are clearly much more significant than that of other pitch angles. During the orbit in Figure 3(c), there are significant fluctuations in both solar wind velocity and density and magnetic fields. Although this orbit shows minimal differences from those in Figures 3(b) and (d), it exhibits multiple crossings of the magnetosheath frequently, represented by lower velocity, higher magnetic field intensity, and broader energy spectrum below 1 keV. This occurrence is probably attributed to brief reconfigurations of the Mars magnetosphere between the two consecutive CMEs. Such temporary recoveries lead to the expansion of the previously compressed magnetopause. The expansion is oscillatory and unstable, which may result in MAVEN repeatedly crossing the bow shock multiple times during this period (C. Bertucci et al. 2005; H. Sui et al. 2023). Due to the brief duration of the bow shock expansion, we did not observe a clear ionospheric response directly associated with it. The response will be further investigated in future studies. In Figure 3(e), as the CME passes by, the solar wind conditions in the vicinity of Mars gradually begin to stabilize. The observations from MAVEN align with the characteristics of a CME event (B. M. Jakosky et al. 2015a) and suggest that the long-lasting SEPs observed by MEPA are attributed to a sequence of two consecutive CMEs. Note that on August 30 at around 12:10 UT and September 1 at around 18:00 UT (the shadow regions in the second image of Figures 3(c) and (e)), an increase in solar wind speed and a decrease in ion density are observed. However, no corresponding changes are detected in the magnetic field intensity and electron pitch-angle distribution by other instruments at the same time. This may due to a mode switch at these two points of time as SWIA has two detection modes including solar wind mode and magnetosheath mode (J. S. Halekas et al. 2013). At the time of mode switching, there is no clear signature of crossing the bow shock, such as the fluctuation of magnetic field and flux spectrogram. Therefore the sudden decrease of solar wind density and increase of solar wind speed at these two incidents are not physical, but an instrumental effect.

In phase V, the energy range of protons decreases, leaving only two narrow energy channels at 2 and 1 keV representing He^{2+} and protons, as shown in the top image of Figure 3(e). This is the hallmark signature of the pristine solar wind (Z. Girazian et al. 2024). In CME events, due to the increase of various ion fluxes, residual He^{2+} slightly increases its flux for a short period of time, resulting in two energy bands.

The data taken by PSP near the Sun are further examined to confirm the detection of CMEs by Tianwen-1 and MAVEN near Mars. Figure 4(a) shows a significant increase in the proton flux of 62 eV to 18 keV on August 27 14:00 UT and an increase to a second peak at 2:00 UT on August 29. The solar wind velocity, density, and magnetic field intensity show the same variation (as shown in Figures 4(b)–(d)). Figure 4(e) illustrates the pitch-angle distributions of 10–200 eV electrons, highlighting the presence of bidirectional streaming of electrons as a typical feature of CME events (C. Shen et al. 2014). Due to the absence of magnetic field data, only the corresponding changes of the second peak are presented, while the variations of other parameters are indicated by the gray and red shaded regions). Using the average velocities of the two leading shock waves and their associated CMEs during this event (618 km s^{-1}), along with the PSP-recorded distance from the Sun and the MAVEN-recorded distance between the Sun and Mars, the estimated propagation time is about 2.9 days from the location of PSP to near-Mars. This is consistent with

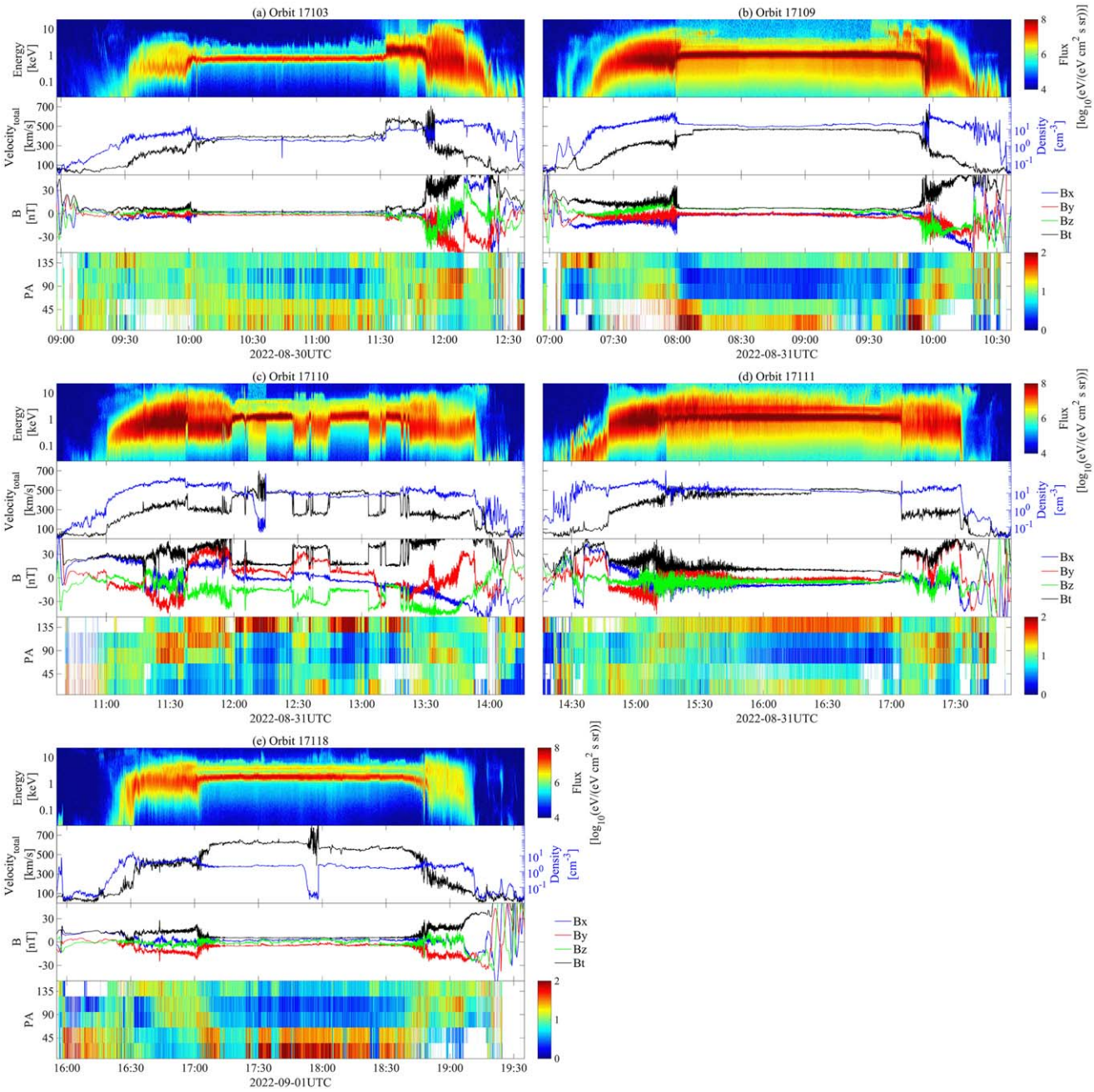

Figure 3. Solar wind condition observed by MAVEN. Each panel shows data of one orbit selected in phase I–V. In each panel, the top image represents the energy spectrum of protons in the energy range of 26 eV to 23 keV; the second image shows the solar wind ion velocity (black line, assuming the ions are solely protons) and proton density (blue line); the third image shows three components (*Bx*, *By*, *Bz*) of the magnetic field in colored lines (the sequence is: blue, red, green) and its magnitude (*Bt*) in black; and the bottom image represents the average pitch-angle distributions of 100–500 eV electrons.

the time difference between the observations. Thus, the consecutive nature of two CMEs observed by Tianwen-1 and MAVEN near Mars is hereby confirmed by the PSP.

Figure 5 shows two snapshots of the WSA-ENLIL simulation result. During a comprehensive simulation that shows the entire propagating process of the CME departing from the Sun and then passing through Mars, we extract the simulation results at two specific times: around 12:00 on 2022 August 27 when the CME passed the PSP, and around 18:00 on 2022 August 29 when it reached the vicinity of Mars. The travel time is several hours short as compared with the recording time of the CME between PSP and Tianwen-1. But this deviation is acceptable in the context of long-duration simulations, especially because we focus more on the structures of CME. In the simulation results, PSP is in the propagation path of CME toward Mars, indicating that the CME observed by PSP is the same one as that detected by Tianwen-1 and MAVEN. As the CME approaches Mars, it is found that Mars may experience two successive enhancements of the solar wind velocity (the contour in Figure 5(b)), consistent with observations of two consecutive impacts of CMEs near Mars.

4. Ionosphere Responses

Following the CME, we turn to investigate the responses in the Martian nightside ionosphere. MAVEN's various orbits enable it to observe distinct regions of Mars (e.g.,

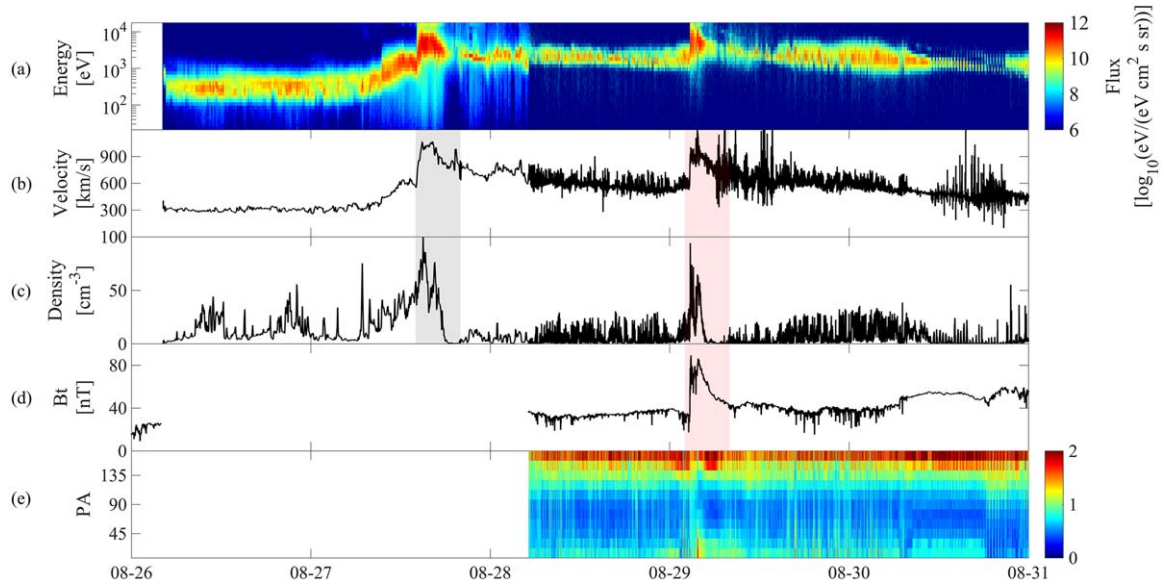

Figure 4. PSP observations: (a) energy spectrogram of low-energy protons from 21 eV–18 keV; (b)–(d) solar wind velocity, solar wind proton density, and the magnitude of magnetic field; and (e) the average pitch-angle distributions of 10–200 eV electrons.

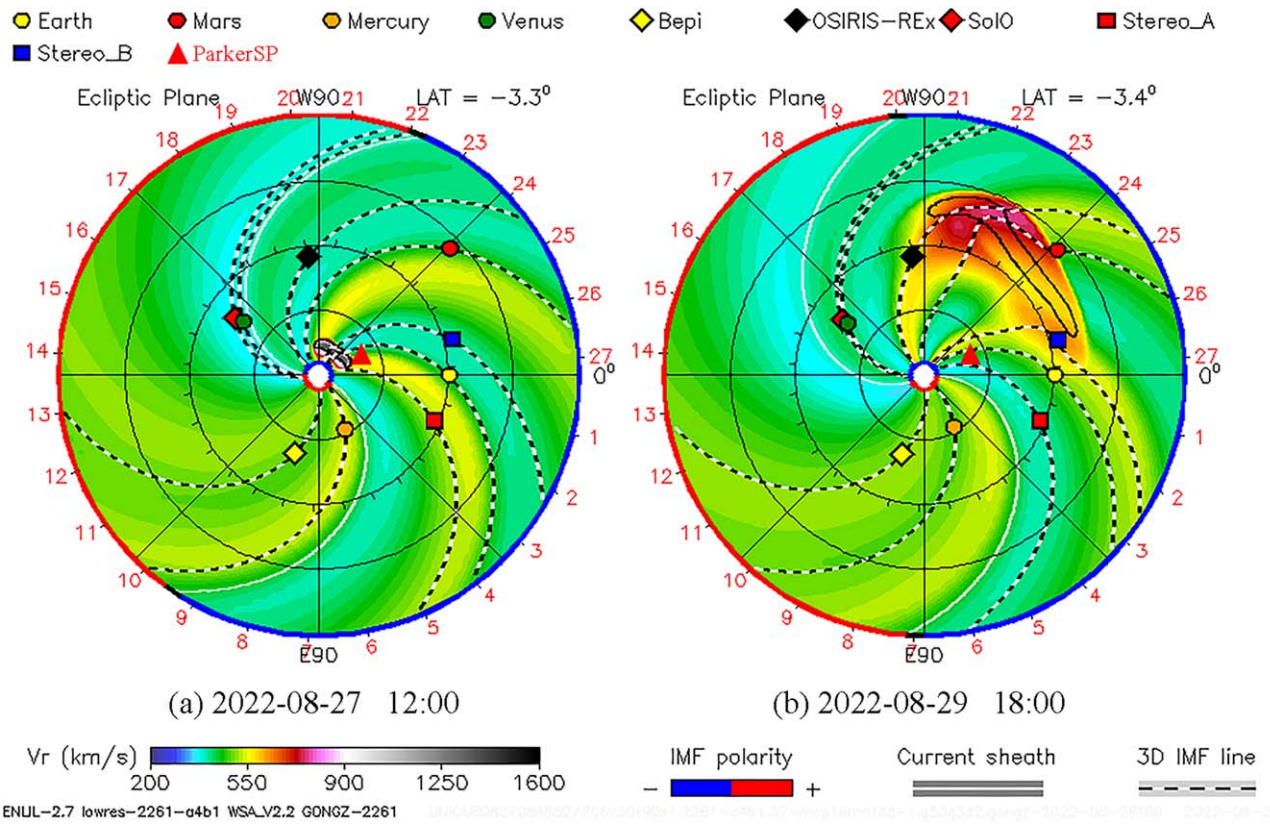

Figure 5. WSA-ENLIL model simulation results of the radial component of solar wind velocity (*Vr*) during the CME event occurred on 2022 August 27: (a) when the CME departed from the Sun approaches the PSP (red triangle) at 12:00 UT on 2022 August 27; (b) the CME reaches the vicinity of Mars (red dot) at 18:00 UT on 2022 August 29.

L. Ram et al. 2023). During the CME event, MAVEN passed through the Martian nightside ionosphere in both hemispheres within approximately 40 orbits (from August 29 to September 3, from phase I to the end of Figure 2(b)), at altitudes ranging from 200 to 500 km, allowing us to explore the responses in the nightside ionosphere as well as to compare the differences between the two hemispheres.

4.1. Ionospheric Profile

According to the five phases of the CME passage, the observations in the ionosphere are also divided into five phases, as shown in Figure 6. The average of the quiet-time ion density from orbit 17094 to 17102 before phase I and from orbit 17123 to 17133 after phase V is used to determine the quiet-time ion-density profiles.

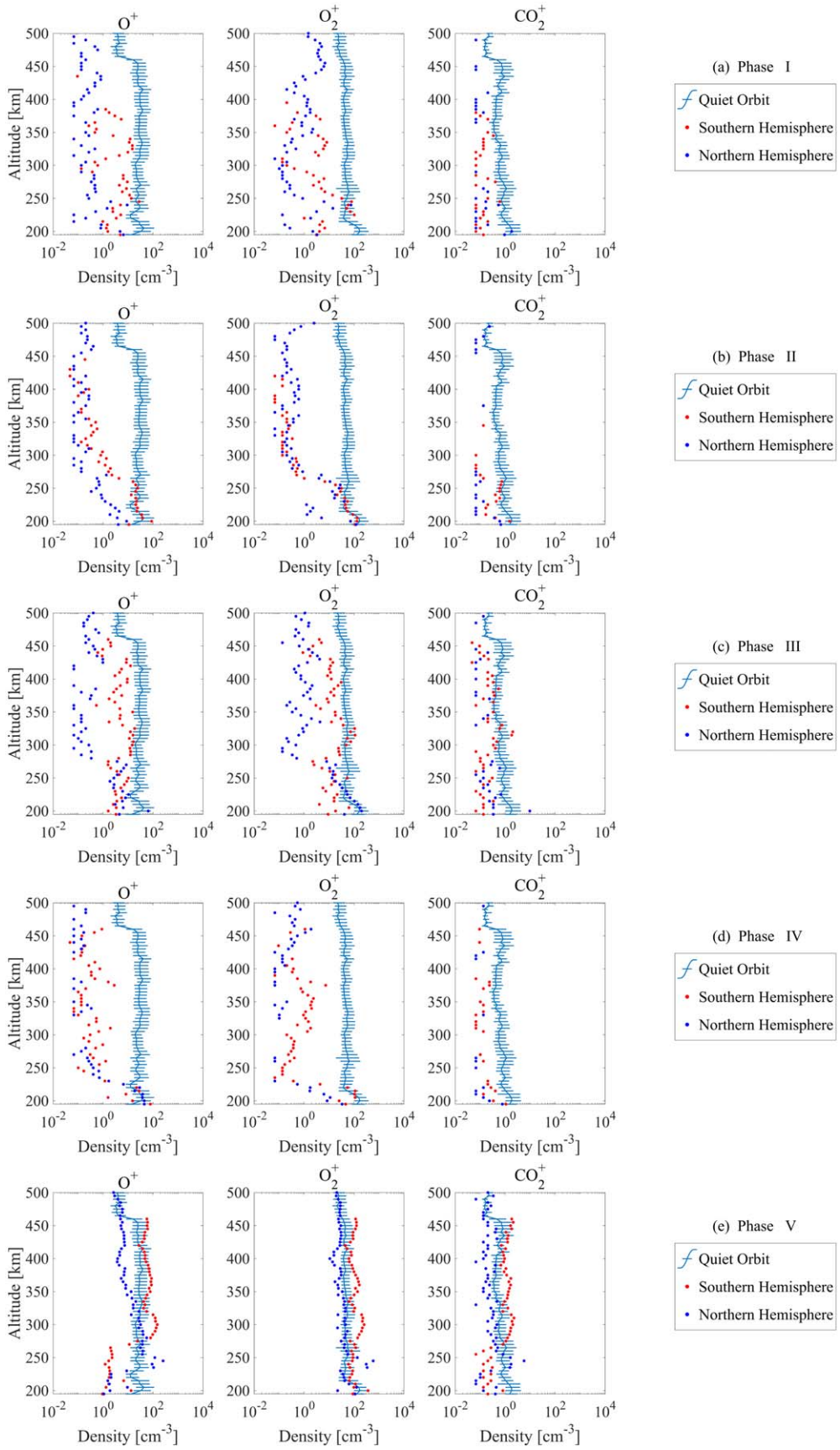

Figure 6. Ionospheric profile from NGIMS/MAVEN measurements: (a)–(e) represent the phases I–V of the event; three subgraphs show the changes in ion density of O^+, O_2^+, and CO_2^+ in each phase. The blue dots represent the ion densities of northern hemisphere, the red dots represent the ion densities of southern hemisphere, and the blue solid line with the error bar represents the quiet state.

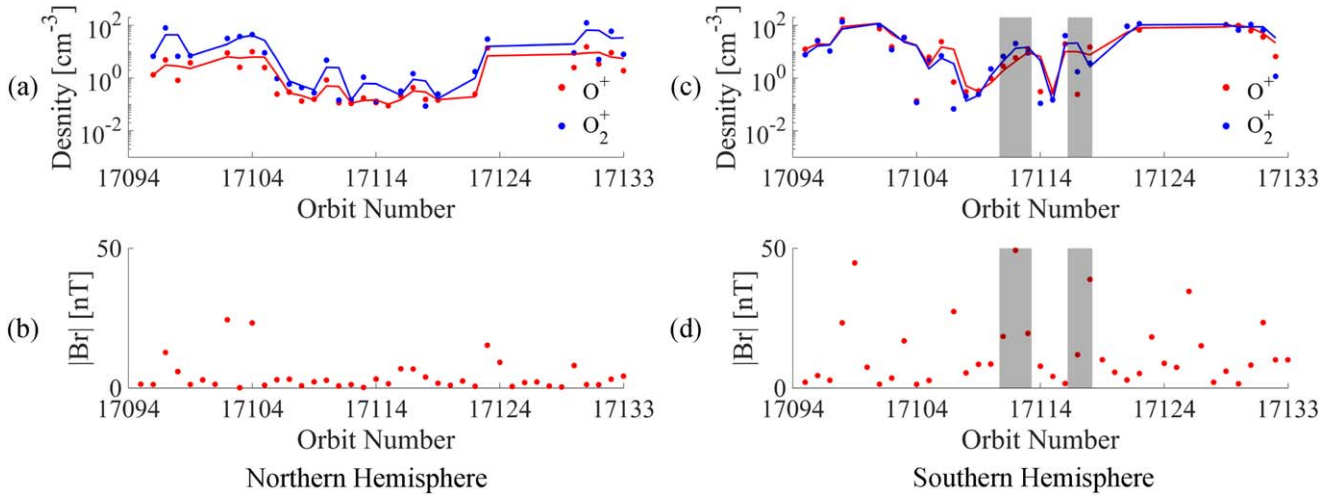

Figure 7. Changes in O^+ and O_2^+ density (the data of key parameters from in situ MAVEN measurements) and absolute value of crustal magnetic field within the altitude range of 300–400 km, (a)–(b) and (c)–(d) represent the northern and southern hemispheres, respectively. In (a) and (c), blue dots indicate O_2^+ while red dots indicate O^+, and the lines derived from the data after smoothing represent their trends of changes. Each dot is obtained from averaging over altitudes ranging from 300 to 400 km. In (b) and (d), red dots indicate the value of the radial component of crustal magnetic field at the median altitude of 350 km simulated by the G110 model. The shadow regions represent areas with a significantly high absolute value of the crustal magnetic field.

In phase I as the start of the event (as shown in Figure 6(a)), the ion densities above 250 km are significantly lower than that in quiet times in both hemispheres, while those below 250 km seem to be comparable. The variations in O^+ and O_2^+ densities above 250 km show a more remarkable reduction in the northern hemisphere than in the southern hemisphere. In the southern hemisphere, ions above 400 km are completely depleted. These observations indicate that O^+ and O_2^+ particles, as the primary components, undergo significant changes in the early phases of CMEs.

As the event progresses, during the Phase II (in Figure 6(b)), the density of O^+ and O_2^+ at various altitudes in the ionosphere continue to decrease, and CO_2^+ is depleted over a broader range of altitude. The ion density above 300 km decreases by about two orders of magnitude compared with the quiet time when the most intense CME hits the Mars system.

In phase III (as shown in Figure 6(c)), there is a slight increase in the densities of O^+ and O_2^+ ions in the northern hemisphere, while the ion density at various altitudes in the southern hemisphere recovers to levels close to the quiet state. During phase IV, the ion density decreases again in multiple orbits. In fact, the nightside ionospheric profiles show similar responses during both phase II and IV (see Figures 6(b) and (d)).

After the event, in phase V, the ion densities nearly recover to the quiet-time level, except those (i.e., O^+, CO_2^+) at low altitudes (<250 km). The densities in the southern hemisphere in general recover to a higher level than that in the northern hemisphere above 250 km (as shown in Figure 6(e)).

The above results suggest a notable correlation between the nightside ionospheric ion-density profile and variations of solar wind conditions. During the August 30 CME event, the two enhancements of energetic proton flux denote the high-level intensity of the event. The associated ionospheric responses also demonstrate ion-density reduction twice, in phase II and IV, respectively. Moreover, it is noted that the reduction of the ion density in the southern hemisphere occurs at a significantly slower rate compared with the northern hemisphere, but the recovery is notably faster. This disparity is probably attributed to the presence of the crustal magnetic field in the southern hemisphere, which inhibits ion movement within the ionosphere and reduces escape rates. The detailed mechanism underlying this effect will be examined in the next section.

4.2. Differences between the Northern and Southern Hemispheres

Figure 7 illustrates the correspondence of the average densities of O^+ and O_2^+ with the crustal magnetic field within the altitude range of 300–400 km in both hemispheres. In the northern hemisphere, both ion densities undergo clear decrease during the CME passage from approximately orbit 17104 (phase II) to orbit 17117 (phase IV), up to two orders of magnitude difference. The ion density in the southern hemisphere notably experiences multiple recoveries (the shaded regions in Figures 7(c) and (d)). When we inspect the in situ magnetic fields, it is found that the magnetic field is occasionally much stronger in the southern hemisphere and appears to correlate well with these brief enhancements of ion density. Given that our observations in Section 4.1 reveal that the averaged ion-density height profiles in the southern hemisphere exhibit slower responses compared with the northern hemisphere, the abrupt increase of density here suggests that the changes in ion density may represent MAVEN's entering a region with higher ion density in ionosphere rather than a temporary recovery of the region where ion density had previously decreased. Instead, Figure 7 illustrates that the region with a strong crustal magnetic field may experience minimal ion-density variation during the CME event, maintaining a relatively high density.

To better understand the different responses of ion density between the northern and southern hemispheres and the influence of crustal magnetic fields, Figure 8 shows the O_2^+ density along orbits within the ionosphere, inbounding from the southern hemisphere and outbounding in northern hemisphere. The radial component of the crustal magnetic field, simulated by the G110 model (J. W. Gao et al. 2021) at a height of 350 km, is shown in the horizontal plane. The radial component of the crustal magnetic field is largely unaffected by the

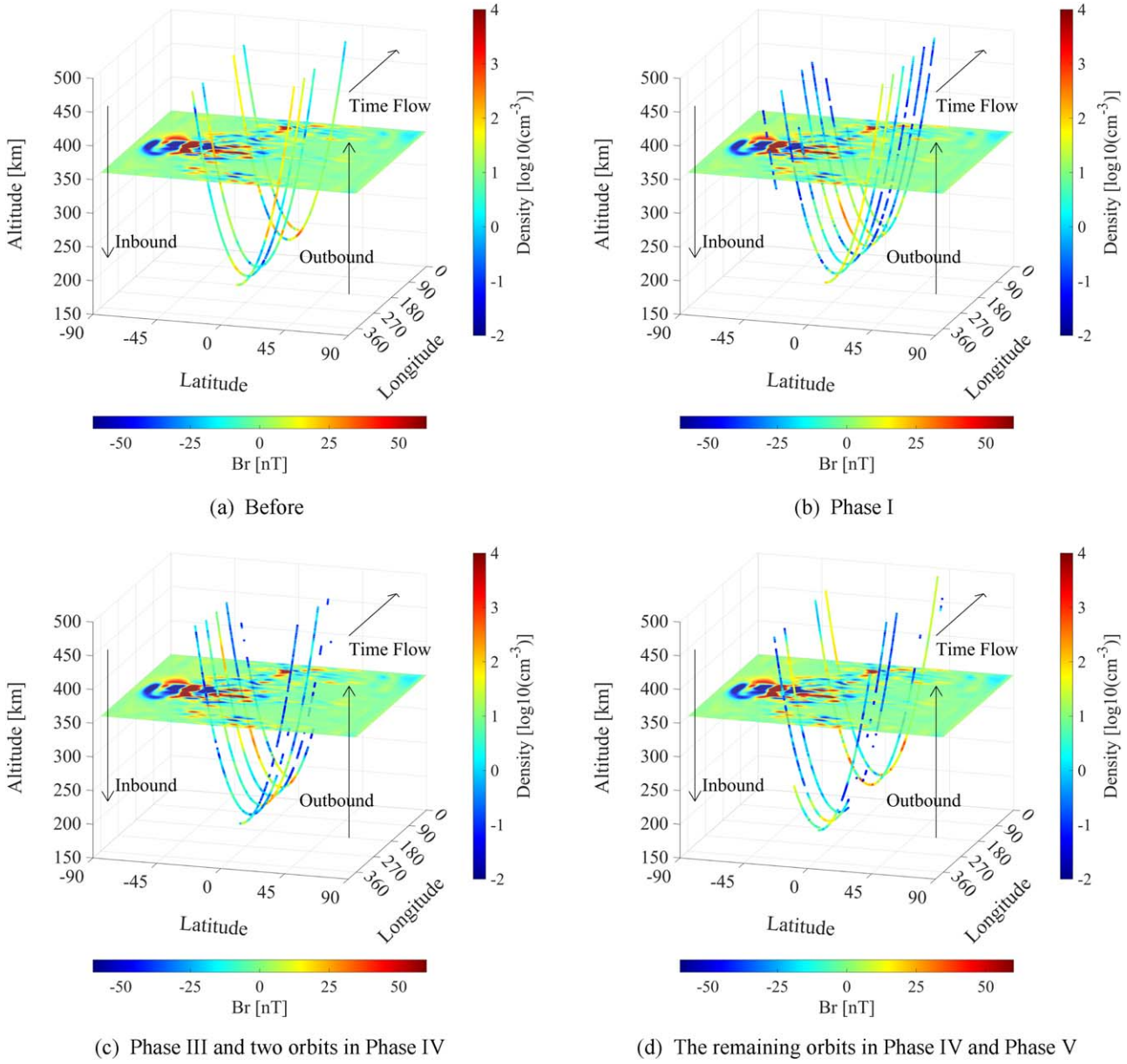

Figure 8. The O_2^+ density and crustal magnetic field distribution are divided into four phases from original five phases: (a) distribution before the event; (b) distribution from the arrival of the event on Mars to phase I; (c) distribution of phase III and two orbits in phase IV; and (d) distribution of the remaining orbits in phase IV and phase V. The vertical colorbar represents ion density, and the horizontal colorbar represents the radial component of crustal magnetic field strength (*Br*).

ionosphere and can serve as a sensitive indicator of the presence of magnetic sources within the crust (M. H. Acuña et al. 1999). Each line represents a segment of a MAVEN's orbit, descending downward below 500 km to the periareion and then rising again. The multiple lines in each figure, arranged with decreasing longitude, correspond to consecutive orbits through the nightside ionosphere. The color on the lines represents O_2^+ ion density. During the passage of the CME (as shown in Figures 8(b) and (c)), the O_2^+ density below 500 km in the northern hemisphere experiences decrease during the first several orbits and continues to maintain at a lower level (in blue). As the CME passes by (i.e., in phase V), the ion density in both hemispheres gradually returns to initial levels (in yellow), as shown in last few orbits in Figure 8(d).

In the latitude and longitude diagram, the crustal magnetic field is mainly distributed in longitude of 120°−270° in the southern hemisphere. Considering the correlation between the crustal magnetic field and the variation of ion density with altitude, longitude, and latitude, it is evident that the crustal magnetic field significantly resists the influence of CME events on the Martian ionosphere. In addition, at higher altitudes, the difference between the northern and southern hemispheres decreases due to the weakening of the crustal magnetic field. It is noted that some orbits lack ion-density data, which may be attributed to the patchy and sporadic nature of the nightside ionosphere (D. Gurnett et al. 2008; Z. Girazian et al. 2017; S. Wu et al. 2023). Through comparative analysis of multiple orbits as discussed above, we are able to conclude that solar activity similar to the August 30 CME event can lead to ion-density reduction in the nightside ionosphere, and the responses in the southern hemisphere is more complicated than northern hemisphere.

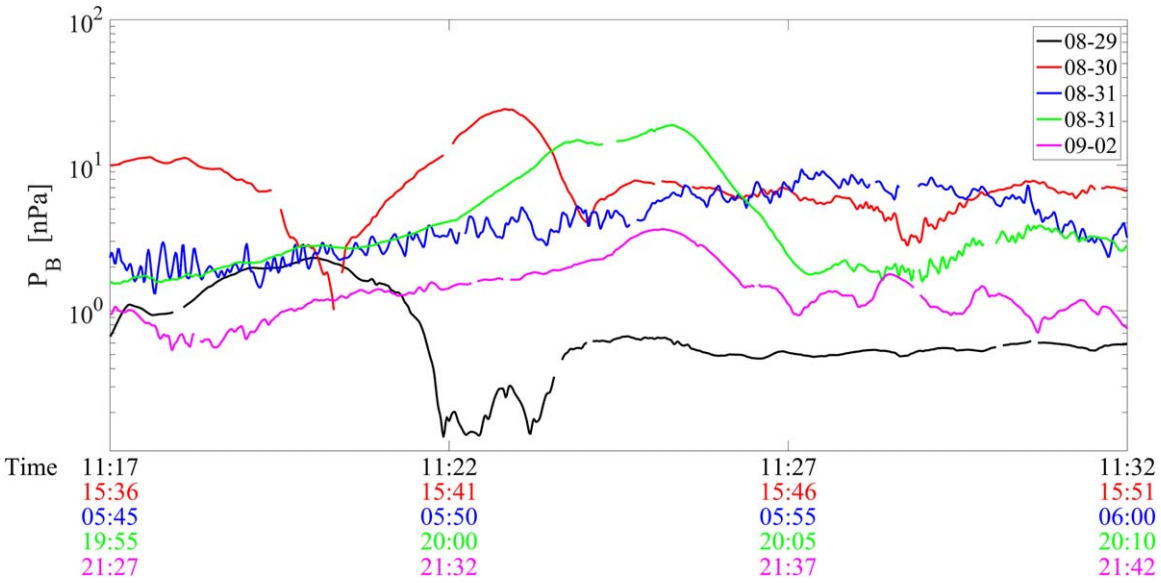

Figure 9. Magnetic pressure observed during one orbit of Tianwen-1 entering the dayside ionosphere below 500 km in the five phases (the magnetic pressure rises at 15:41 on August 30 and 20:04 on August 31, corresponding to the time points of the red and green lines in Figures 2(b) and (c)).

5. Discussion and Conclusion

In this study, we utilize joint observational data from two instruments (SPAN Ion instrument and Electron instrument) on board the PSP spacecraft, two instruments (MEPA and MOMAG) on board the Tianwen-1 mission, and three instruments (SWEA, SWIA and NGIMS) on board the MAVEN spacecraft to investigate the ionospheric responses to a CME event that occurred on 2022 August 30.

To understand the reasons for the decrease of ion density in the night ionosphere, it is necessary to investigate the sources and losses of these ions. The Martian nightside ionosphere during CME events experiences loss primarily through mechanisms such as bulk ion loss, ionospheric ion outflow, and solar wind pickup (H. J. Opgenoorth et al. 2013). The complexities of ion escape mechanisms and rates have been extensively studied (e.g., M. W. Liemohn et al. 2013; H. Gröller et al. 2014; D. A. Brain et al. 2015). This paper aims to explain the response of the nightside ionosphere by discussing the impact of CMEs on its sources. It is widely accepted that the main sources of the nightside ionosphere are the day-to-night transport of particles and the impact ionization of deposited electrons (J. Cui et al. 2015; D. Adams et al. 2018). However, in the study by D. Adams et al. (2018) and Y. Cao et al. (2019), it was shown that electron impact ionization is the main source for low altitude (<200 km) plasma, while day-to-night transport is the main source of high-altitude plasma. In our study, MAVEN passes through high-altitude ionosphere, which is unlikely affected by the penetrated impact ionization. Therefore, we focus on the mechanism of day-to-night particle transport.

In fact, when the solar wind dynamic pressure increases, the main force that balances the solar wind dynamic pressure in the Martian magnetic pile-up boundary (MPB) region and the magnetosphere is magnetic pressure (D. H. Crider et al. 2003). According to the study by X. Wu et al. (2019), based on the momentum equation of a certain steady-state ion on Mars, the force conditions of this ion includes ion thermal pressure, bipolar electric field, local gravity, and magnetic pressure term. The total vertical force per ion contributed by these four items could be written as

$$f_i = -\frac{1}{n_i}\frac{d(n_i k T_i)}{dz} - \frac{1}{n_e}\frac{d(n_e k T_e)}{dz} - m_i g - \frac{1}{n_e}\frac{d}{dz}\left(\frac{B_h^2}{8\pi}\right), \tag{3}$$

where z represents the altitude; n_i and n_e are the ion and electron number densities; T_i and T_e are the ion and electron temperatures; m_i, k and g represent the ion mass, the Boltzmann constant, and the local gravity, respectively; and B_h represents the horizontal magnetic field strength.

After statistical and simulation studies, it has been found that magnetic pressure plays the most important role in the force exerted on ionospheric ions (X. Wu et al. 2019). Figure 9 shows the observed magnetic pressure by Tianwen-1 on the dayside in different orbits (utilizes the spacecraft altitude below 500 km as a brief delineation). We briefly estimated the averaged variation of solar wind dynamic pressure from Phase I to V by the solar wind data of SWIA/MAVEN. During phases II and IV, the dynamic pressure was 6–7 times that of the quiet period, with values between 4.2 and 5.1 nPa. Phase III exhibited a brief decline, yet remained approximately four times that of the quiet period, at 2.9 nPa. Correspondingly, the magnetic pressure in the ionosphere below 500 km, as shown in Figure 9, demonstrates an increase–decrease–increase-recovery pattern. The magnetic pressure rises to the first peak at 15:41 UT on August 30 (red) in phase II and rises again at 20:04 UT on August 31 (green), corresponding to the vertical lines in Figure 2(b) in phase II and IV. These changes are observed around 4 hr after the observation of peaked proton flux, which is attributed to Tianwen-1 detecting the proton flux in the solar wind before entering the dayside ionosphere. Therefore, we can conclude that the increase in magnetic pressure during phases II and IV, as well as the decrease during phases III and V, corresponds well to the variations in the solar wind dynamic pressure and consequently the ionospheric response.

This suggests that the underlying mechanism may be associated with the increase in magnetic pressure on the dayside, which drives a higher ion escape rate, increasing

pickup ion escape and enhancing ion outflow (X. Wu et al. 2019). As a result, the top ionosphere was largely depleted (T. E. Cravens et al. 2017; J. S. Halekas et al. 2017b; X. Wu et al. 2019). As the CME arrived near Mars, the enhanced solar wind dynamic pressure compressed the bow shock, MPB, induced magnetosphere, and even the ionosphere. This process makes the dayside ionosphere a smaller reservoir of plasma that can be transported anti-sunward to replenish the high-altitude nightside ionosphere, thus resulting in a decrease of ion density in the nightside ionosphere.

As for the high-level ion density in the southern hemisphere, the observations (as shown in Figures 7 and 8) indicate that these regions are featured by strong crustal magnetic fields. During CME events, the ion density in regions with strong crustal magnetic fields exhibits slower responses and smaller variations compared with other regions. This phenomenon is probably attributed to the fact that in regions with strong crustal magnetic fields, the influence of ion transport is minimized due to the magnetic structure (Y. Cao et al. 2019). A significant portion of the charged ions is trapped by the crustal magnetic field and is subsequently cycled within the mini-magnetospheres generated by the Martian small-scale planetary crustal fields (R. Lundin et al. 2011; Z. Girazian et al. 2017; E. Dubinin et al. 2020). Therefore, although the passage of CMEs reduces the ion sources from dayside, regions with stronger crustal magnetic fields on the nightside are less affected and experience changes more slowly. Only after a certain duration does the decrease in ion sources significantly impact these areas, causing ion density to drop to levels comparable to those in the northern hemisphere (E. Dubinin et al. 2020; A. Mittelholz & C. L. Johnson 2022). In Figure 6(e), we noted that the densities of O^+ and CO_2^+ are lower than that in quiet state below 250 km. This is probably because during the day-to-night transport, these ions may undergo more significant conversion to O_2^+ via ion-neutral chemistry (reaction Equations (1) and (2)) due to a higher abundance of the ambient neutrals at low altitudes (S. A. Haider 1997).

In summary, analysis of the August 30 CME event demonstrates that the response of the Martian ionosphere is highly associated with the CME intensity and solar wind conditions, such as proton flux and solar wind speed. The ion density on the nightside in the altitude of 200–500 km decreases with the intensity of the CME event. The CME event, accompanied with increased solar wind dynamic pressure, compresses the Martian plasma environment and enhances the magnetic field and pressure, resulting in profound ion escape in the dayside ionosphere. The day-to-night transport, as the primary source of the nightside ionosphere at this altitude, therefore carries less ion sources to the nightside, leading to a significant decrease of the main ions of the nightside ionosphere. Furthermore, the nightside ionosphere in the northern and southern hemispheres exhibits distinct responses. The influence of the crustal magnetic field results in a slower variation in ion density in the nightside ionosphere of the southern hemisphere compared with that of the northern hemisphere.

Previous studies on the effects of CME events on the Martian upper ionosphere primarily focused on the rough impacts on the dayside and nightside ionospheric profiles, with relatively simplistic descriptions of their dependence on solar activity and crustal magnetic field (L. Ram et al. 2023; B. Yu et al. 2023). They concluded that CME events led to a reduction in ion density in the ionosphere and identified differences in the impacts of various events. However, the explanations regarding the differences and mechanisms affecting the northern and southern hemispheres of the Martian nightside ionosphere due to CME events are insufficiently comprehensive. Our study, aided by joint observations of the Tianwen-1 and MAVEN missions, comprehends the impact of a CME event on various regions of Mars and its underlying mechanisms.

Acknowledgments

This work was supported by the National Natural Science Foundation of China (NSFC) grants 42350710793 and 41821003, and by the Fundamental Research Funds for the Central Universities. We sincerely acknowledge the MAVEN team for the data. All the data of MAVEN and the level-3 data of PSP are obtained from https://cdaweb.gsfc.nasa.gov/. The PDS Planetary Plasma Interactions Node (https://pds-ppi.igpp.ucla.edu/) makes the MAVEN data publicly available; specifically, the MAG data (J. Connerney 2017), the SWIA data (J. Halekas 2017a, 2017b), the SWEA data (D. Mitchell et al. 2016) and the NGIMS data (M. Elrod et al. 2014) are available. We also acknowledge the Community Coordinated Modeling Center (CCMC) at Goddard Space Flight Center for the WSA-ENLIL +CONE Model for simulation snapshots of the ISWA Data Tree, https://iswa.ccmc.gsfc.nasa.gov/iswa_data_tree/. MEPA data processing work is supported by the introduction to data processing methods provided by Science and Technology on Vacuum Technology and Physics Laboratory, Lanzhou Institute of Physics. The files contain calibrated level-2B data of MEPA of Tianwen-1 can be downloaded from the Lunar and Planetary Data Release System at National Astronomical Observatories of China: https://moon.bao.ac.cn/web/zhmanager/mars1. The data of MOMAG of Tianwen-1 can be obtained at the official website of the MOMAG team: https://space.ustc.edu.cn/dreams/tw1_momag/.

ORCID iDs

Longhui Liu https://orcid.org/0009-0009-6971-4945
Xinzhi Qiu https://orcid.org/0000-0002-6237-701X
Yiqun Yu https://orcid.org/0000-0002-1013-6505
Jinbin Cao https://orcid.org/0000-0002-5637-2976
Cunhui Li https://orcid.org/0000-0003-2689-9387
YuMing Wang https://orcid.org/0000-0002-8887-3919

References

Acuña, M. H., Connerney, J. E. P., Ness, N. F., et al. 1999, Sci, 284, 790
Adams, D., Xu, S., Mitchell, D., et al. 2018, GeoRL, 45, 12,190
Arge, C. N., & Pizzo, V. J. 2000, JGR, 105, 10465
Bertucci, C., Mazelle, C., & Acuña, M. 2005, AdSpR, 36, 2066
Brain, D. A., McFadden, J. P., Halekas, J. S., et al. 2015, GeoRL, 42, 9142
Burch, J., Torbert, R., Phan, T., et al. 2016, Sci, 352, aaf2939
Cane, H. V., Reames, D. V., & von Rosenvinge, T. T. 1988, JGR, 93, 9555
Cao, Y., Cui, J., Wu, X., Guo, J., & Wei, Y. 2019, JGRE, 124, 1495
Chen, P. F. 2011, LRSP, 8, 1
Chen, R. H., Cravens, T. E., & Nagy, A. F. 1978, JGR, 83, 3871
Chi, Y., Shen, C., Cheng, L., et al. 2023, ApJS, 267, 3
Connerney, J. 2017, urn:nasa:pds:maven.mag.calibrated:data.ss::2.32, NASA Planetary Data System, doi:10.17189/1414251
Connerney, J. E. P., Espley, J., Lawton, P., et al. 2015, SSRv, 195, 257
Cravens, T. E., Hamil, O., Houston, S., et al. 2017, JGRA, 122, 10,626
Crider, D. H., Vignes, D., Krymskii, A. M., et al. 2003, JGRA, 108, 1461
Cui, J., Galand, M., Yelle, R. V., Wei, Y., & Zhang, S. 2015, JGRA, 120, 2333
Dubinin, E., Fraenz, M., Andrews, D., & Morgan, D. 2016, P&SS, 124, 62
Dubinin, E., Fraenz, M., Woch, J., et al. 2012, EP&S, 64, 113
Dubinin, E., Fränz, M., Pätzold, M., et al. 2020, JGRA, 125, e2020JA028010

Duru, F., Gurnett, D., Morgan, D., et al. 2017, P&SS, 145, 28
Elrod, M., Benna, M., & Navas, T. 2014, urn:nasa:pds:maven_ngims::1.0, NASA Planetary Data System, doi:10.17189/1518931
Fox, N., Velli, M., Bale, S., et al. 2016, SSRv, 204, 7
Fu, S., Ding, Z., Zhang, Y., et al. 2022, ApJL, 934, L15
Gao, J. W., Rong, Z. J., Klinger, L., et al. 2021, E&SS, 8, e01860
Girazian, Z., Halekas, J., & Ruhunusiri, S. 2024, JGRA, 129, e2023JA032164
Girazian, Z., Mahaffy, P. R., Lillis, R. J., et al. 2017, JGRA, 122, 4712
Gopalswamy, N., Lara, A., Lepping, R. P., et al. 2000, GeoRL, 27, 145
Gröller, H., Lichtenegger, H., Lammer, H., & Shematovich, V. I. 2014, P&SS, 98, 93
Gurnett, D., Huff, R., Morgan, D., et al. 2008, AdSpR, 41, 1335
Haider, S. A. 1997, JGR, 102, 407
Halekas, J. 2017a, urn:nasa:pds:maven.swia.calibrated:data.onboard_svy_spec::1.11, NASA Planetary Data System, doi:10.17189/1414248
Halekas, J. 2017b, urn:nasa:pds:maven.swia.calibrated:data.onboard_svy_mom::1.11, NASA Planetary Data System, doi:10.17189/1414246
Halekas, J., Brain, D., Luhmann, J., et al. 2017a, JGRA, 122, 11,320
Halekas, J. S., Ruhunusiri, S., Harada, Y., et al. 2017b, JGRA, 122, 547
Halekas, J. S., Taylor, E. R., Dalton, G., et al. 2013, SSRv, 195, 125
Hanson, W. B., Sanatani, S., & Zuccaro, D. R. 1977, JGR, 82, 4351
Harada, Y., Gurnett, D. A., Kopf, A. J., et al. 2018, GeoRL, 45, 7960
Hess, P., & Zhang, J. 2017, SoPh, 292, 80
Jakosky, B. M., Grebowsky, J. M., Luhmann, J. G., et al. 2015a, Sci, 350, aad0210
Jakosky, B. M., Lin, R. P., Grebowsky, J. M., et al. 2015b, SSRv, 195, 3
Li, C., Tang, S., Hu, X., et al. 2021, SSRv, 217, 6
Liemohn, M. W., Curry, S. M., Fang, X., & Ma, Y. 2013, JGRA, 118, 4093
Lin, R., Huang, S., Yuan, Z., et al. 2024, GeoRL, 51, e2024GL108880
Liu, K., Hao, X., Li, Y., et al. 2020, E&PP, 4, 384
Livi, R., Larson, D. E., Kasper, J. C., et al. 2022, ApJ, 938, 138
Lundin, R., Barabash, S., Yamauchi, M., Nilsson, H., & Brain, D. 2011, GeoRL, 38, L02102
Mahaffy, P. R., Benna, M., King, T., et al. 2015, SSRv, 195, 49
Mays, M., Taktakishvili, A., Pulkkinen, A., et al. 2015, SoPh, 290, 1775
Mitchell, D., Mazelle, C., Sauvaud, J.-A., et al. 2016, SSRv, 200, 495
Mittelholz, A., & Johnson, C. L. 2022, FrASS, 9, 495
Moore, T. E., Peterson, W. K., Russell, C. T., et al. 1999, GeoRL, 26, 2339
Odstrcil, D. 2003, AdSpR, 32, 497
Odstrčil, D., & Pizzo, V. 1999, JGR, 104, 483
Opgenoorth, H. J., Andrews, D. J., Fränz, M., et al. 2013, JGRA, 118, 6558
Qiu, X., Yu, Y., Gong, F., et al. 2024a, ApJ, 960, 99
Qiu, X., Yu, Y., Wang, J., et al. 2024b, ApJ, 977, 109
Ram, L., Rout, D., Rathi, R., et al. 2023, JGRE, 128, e2022JE007649
Reames, D. V., Kahler, S. W., & Ng, C. K. 1997, ApJ, 491, 414
Russell, C. T., & Shinde, A. A. 2005, SoPh, 229, 323
Semkova, J., Koleva, R., Benghin, V., et al. 2023, LSSR, 39, 106
Shen, C., Wang, Y., Pan, Z., et al. 2014, JGRA, 119, 5107
Shen, F., Shen, C., Xu, M., et al. 2022, RvMPP, 6, 8
Sui, H., Wang, M., Lu, J., Zhou, Y., & Wang, J. 2023, ApJ, 945, 136
Tang, S., Wang, Y., Zhao, H., et al. 2020, E&PP, 4, 355
Thampi, S. V., Krishnaprasad, C., Bhardwaj, A., et al. 2018, JGRA, 123, 6917
Tóth, G., & Odstrčil, D. 1996, JCoPh, 128, 82
Trotignon, J., Mazelle, C., Bertucci, C., & Acuña, M. 2006, P&SS, 54, 357
Ulusen, D., Brain, D. A., Luhmann, J. G., & Mitchell, D. L. 2012, JGRA, 117, A12306
Wang, C., Rosen, I. G., Tsurutani, B. T., et al. 2016, JSWSC, 6, A5
Wang, G., Xiao, S., Wu, M., et al. 2024, JGRA, 129, e2023JA031757
Wang, Y., Wang, B., Shen, C., Shen, F., & Lugaz, N. 2014, JGRA, 119, 5117
Wang, Y., Zhang, T., Wang, G., et al. 2023, E&PP, 7, 216
Whittlesey, P. L., Larson, D. E., Kasper, J. C., et al. 2020, ApJS, 246, 74
Wimmer-Schweingruber, R. F., Crooker, N. U., Balogh, A., et al. 2006, SSRv, 123, 177
Withers, P. 2009, AdSpR, 44, 277
Wu, S., Wu, X., Cui, J., et al. 2023, ApJ, 943, 154
Wu, X., Cui, J., Xu, S. S., et al. 2019, JGRE, 124, 734
Yu, B., Chi, Y., Owens, M., et al. 2023, ApJ, 953, 105
Zhang, J., Guo, J., Zhang, Y., et al. 2024, GeoRL, 51, e2024GL111775
Zou, Y., Zhu, Y., Bai, Y., et al. 2021, AdSpR, 67, 812
Zou, Z., Wang, Y., Zhang, T., et al. 2023, ScChE, 66, 2396